Branched Siloxane Axial Substituents Outperform Linear Analogues in a Model Silicon Phthalocyanine-based Organic Thin Film Transistor

Nicolas Ledos,[1,2] Halynne R. Lamontagne,[1,2] Joseph Manion,[1] Jaclyn L. Brusso.[2,*], and Benoît H. Lessard,[1,3,*]

1. Department of Chemical and Biological Engineering, University of Ottawa, 161 Louis Pasteur, Ottawa, Ontario K1N 6N5, Canada.
2. Department of Chemistry and Biomolecular Sciences, University of Ottawa, 150 Louis Pasteur, Ottawa, ON, Canada, K1N 6N5
3. School of Electrical Engineering and Computer Science, University of Ottawa, 800 King Edward Ave. Ottawa, Ontario K1N 6N5, Canada.

*Corresponding author: benoit.lessard@uottawa.ca (BHL) and jbrusso@uottawa.ca (JLB)

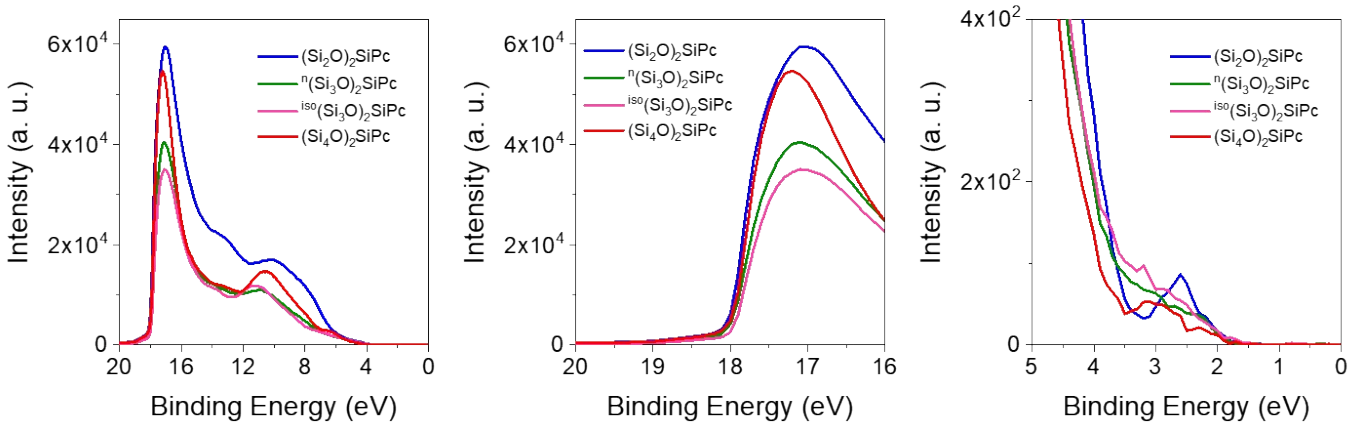

Figure S1: UPS spectrum of $(Si_xO)_2SiPcs$ thin film with a +9V bias and 21.22 eV emission source and calibrated using an Au reference (left). Zoom on the cutoff energy (middle). Zoom on the inset of the trailing edge of the spectrum (right). Data for **$^{iso}(Si_3O)_2SiPc$** were taken from Ledos et al.[1]

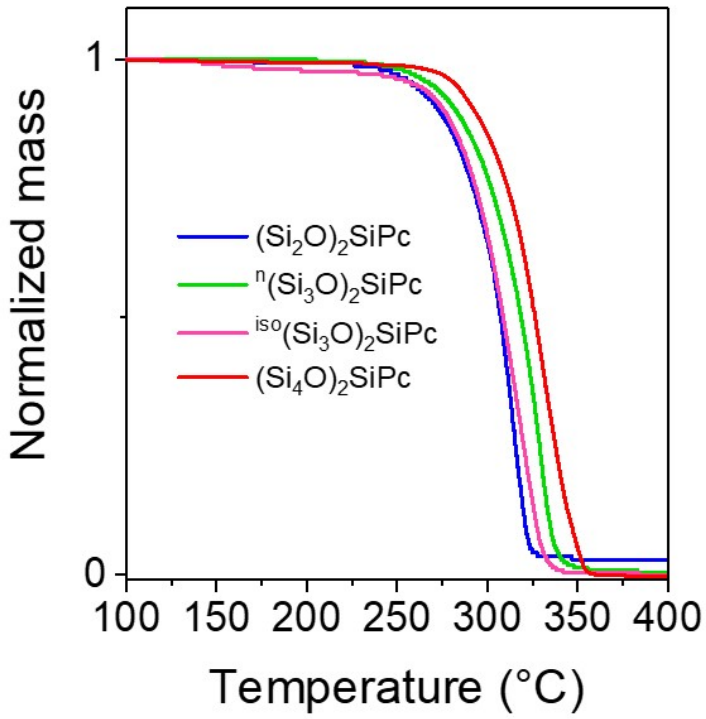

Figure S2: Thermogravimetric analysis of $(Si_XO)_2SiPcs$. Data for **$^{iso}(Si_3O)_2SiPc$** were taken from Ledos et al.[1]

Previous thermal gravimetric analysis (TGA) studies on **$^{iso}(Si_3O)_2SiPc$**, revealed a relatively low sublimation temperature of 260°C and a direct transition from solid to gas phase at ambient pressure which differs from alkylated SiPc based derivatives which appear to melt prior to vaporizing.[2–5] This peculiar behavior was attributed to the presence of siloxane axial substituents,[1] which motivated us to investigate the thermal properties of a new class of $(Si_XO)_2SiPc$ derivatives via TGA under a nitrogen atmosphere. At atmospheric pressure, mass loss (5% loss) begins around 260°C for **$(Si_2O)_2SiPc$**, 270°C for **$^{n}(Si_3O)_2SiPc$** and 280°C for **$(Si_4O)_2SiPc$** (**Figure 2**). In addition, optical microscopy conducted on a heated stage revealed that these compounds had evaporated at these temperatures. For **$(Si_2O)_2SiPc$** and **$^{n}(Si_3O)_2SiPc$** a direct transition from the solid state to the gas phase was observed while for **$^{n}(Si_3O)_2SiPc$** a melting process was observed at 190°C. Therefore, the presence of a siloxane axial substituent on SiPcs can effectively lower their sublimation/evaporation temperature. One can note that the influence of chain branching and length is similar to alkyl chains: an elongated chain displays a higher boiling point compared to a shorter chain and a linear chain displays a lower melting point as well as a higher boiling point compared to a branched chain.[6]

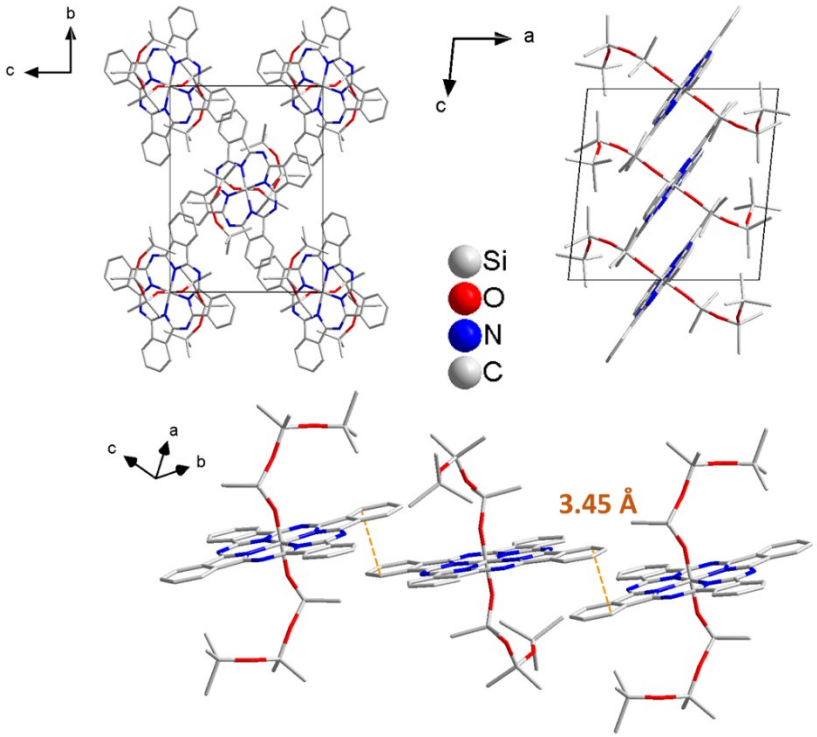

Figure S3: Capped sticks representation of the crystal packing of **^{n}(Si$_3$O)$_2$SiPc** polymorph 1 (CCDC deposit #2487841) viewed along the *a*-axis (top left) and the *b*-axis (top right). Capped sticks representation with the closest C-C distance between the Pc rings highlighted in the orange dash lines (bottom). Hydrogen atoms were omitted for clarity.

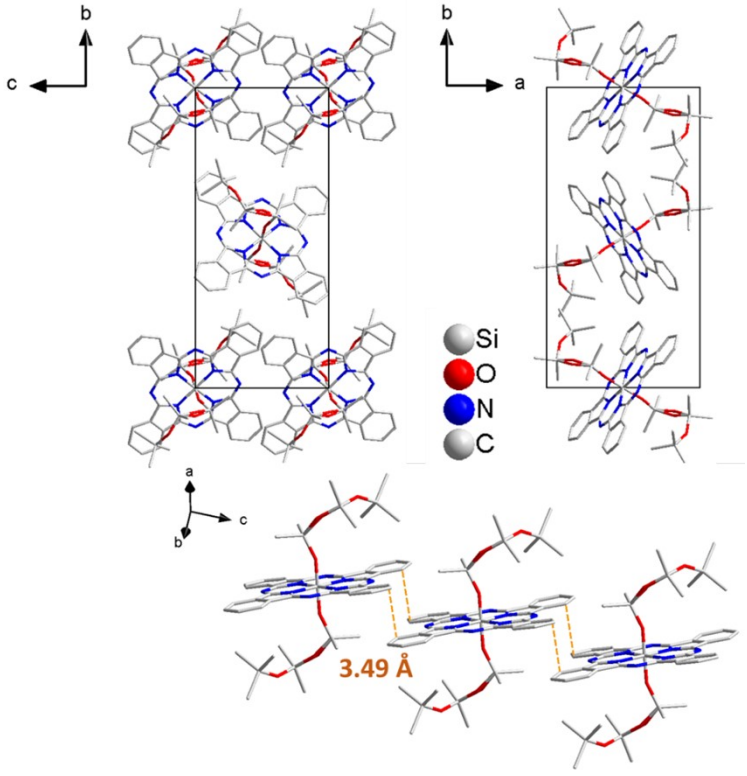

Figure S4: Capped sticks representation of the crystal packing of **^{n}(Si$_3$O)$_2$SiPc** polymorph 2 (CCDC deposit #2487842) viewed along the *a*-axis (top left) and the *c*-axis (top right). Capped sticks representation with the closest C-C distance between the Pc rings highlighted in the orange dash lines (bottom). Hydrogen atoms were omitted for clarity.

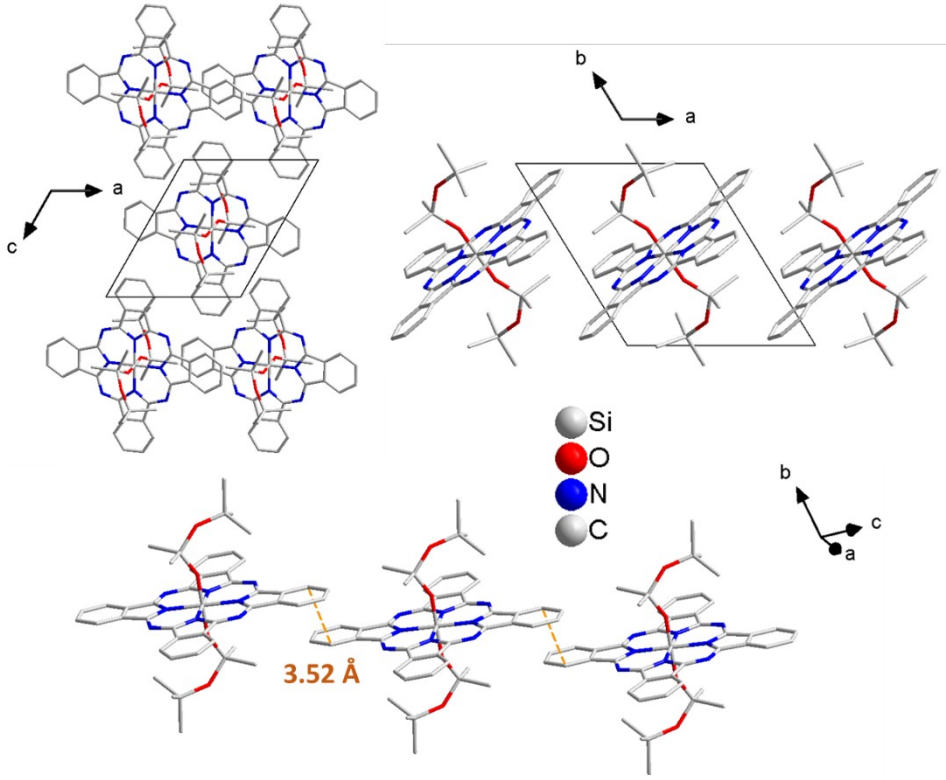

Figure S5: Capped sticks representation of the crystal packing of **$(Si_2O)_2SiPc$** (CCDC deposit #2487844) viewed along the *b*-axis (top left) and the *c*-axis (top right). Capped sticks representation with the closest C-C distance between the Pc rings highlighted in the orange dash lines (bottom). Hydrogen atoms were omitted for clarity.

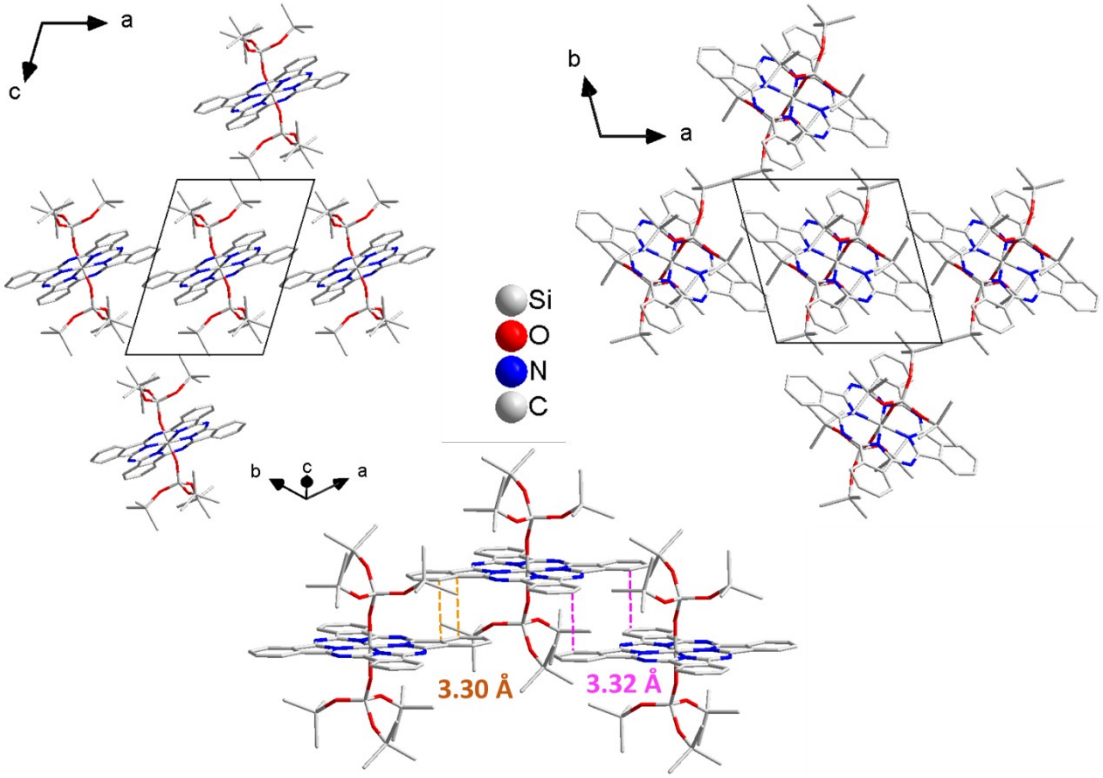

Figure S6: Capped sticks representation of the crystal packing of **$(Si_4O)_2SiPc$** (CCDC deposit #2487846) viewed along the *b*-axis (top left) and the *c*-axis (top right). Capped sticks representation of the closest C-C distance between the Pc rings, the orange dash lines represent the closest C-C distance along the *a*-axis, and the pink dash line represent the closest C-C distance along the *b*-axis. Hydrogen atoms were omitted for clarity.

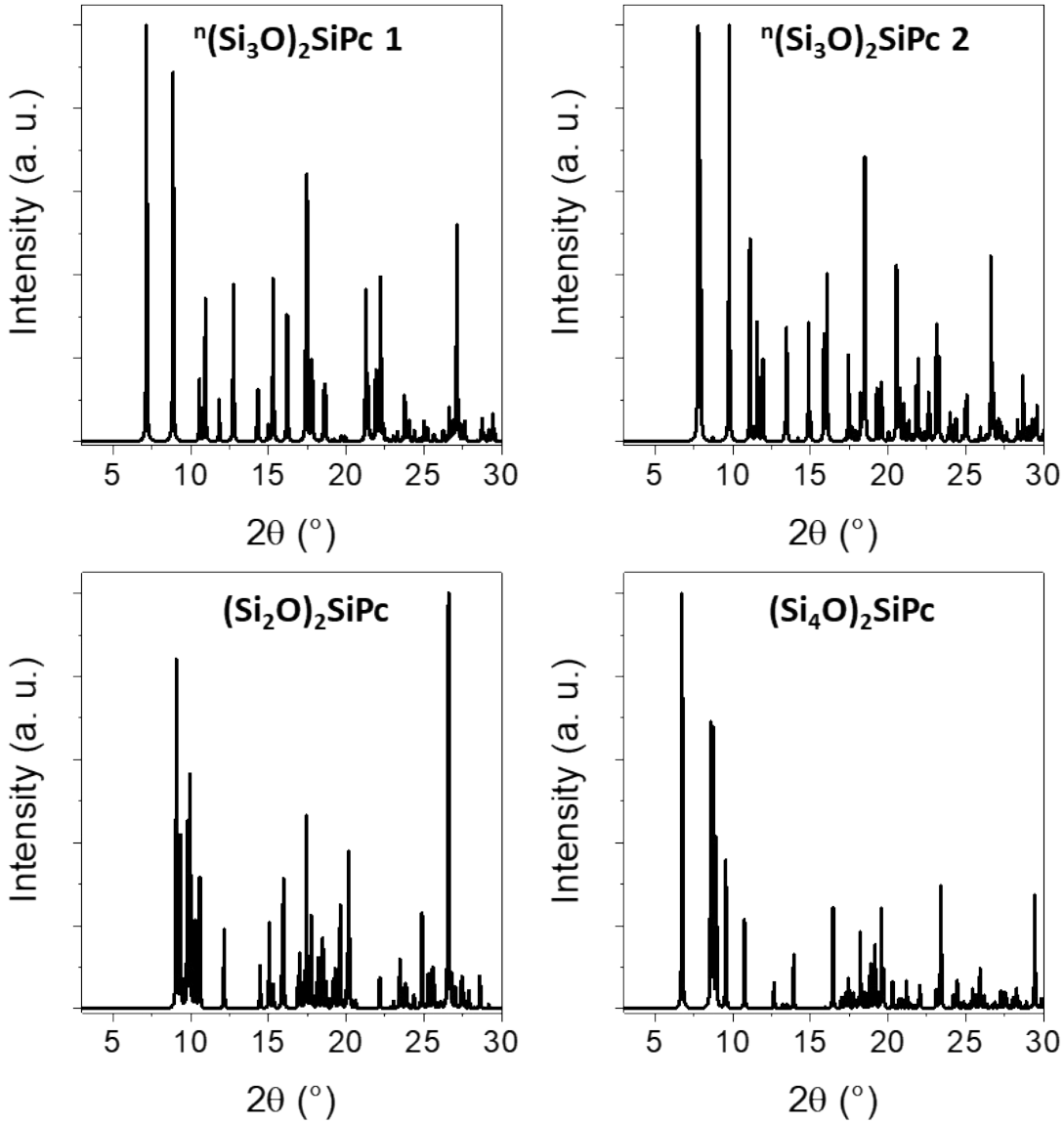

Figure S7: Predicted powder X-ray diffractogram of **ⁿ(Si₃O)₂SiPc** polymorph 1 (top left), **ⁿ(Si₃O)₂SiPc** polymorph 2 (top right), **(Si₂O)₂SiPc** (bottom left) and **(Si₄O)₂SiPc** (bottom right).

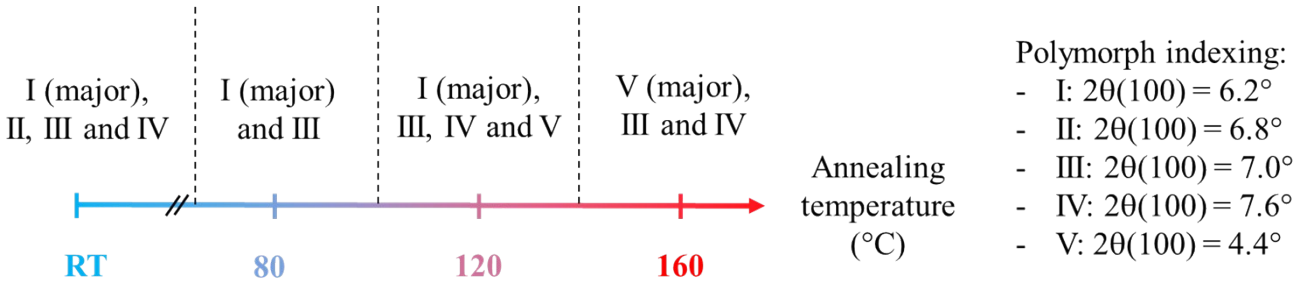

Figure S8: Crystalline phase diagram of **ⁿ(Si₃O)₂SiPc**. Evolution of the polymorphism in thin films upon thermal annealing.

Compound	**$^{n}(Si_3O)_2SiPc$** polymorph 1 CCDC#2487841	**$^{n}(Si_3O)_2SiPc$** polymorph 2 CCDC#2487842	**$(Si_2O)_2SiPc$** CCDC#2487844	**$(Si_4O)_2SiPc$** CCDC#2487846
Formula	C46 H58 N8 O6 Si7	C46 H58 N8 O6 Si7	C42 H46 N8 O4 Si5	C50 H70 N8 O8 Si9
MW	1015.63	1015.63	867.32	1163.95
a (Å)	*12.4104(17)*	*11.5203(4)*	*10.5878(15)*	*10.4508(16)*
b (Å)	*16.745(2)*	*22.3188(7)*	*11.2622(16)*	*11.2504(18)*
c (Å)	*12.4848(17)*	*10.0255(3)*	*11.3535(17)*	*14.665(2)*
α (°)	90	90	99.298(2)	111.132(3)
β (°)	95.725(3)	99.047(2)	112.068(2)	101.618(3)
γ (°)	90	90	114.731(2)	99.430(3)
V (Å^3)	*2581.6(6)*	*2545.68(14)*	*1054.7(3)*	*1521.7(4)*
Z	*2*	*2*	*1*	*1*
*D*c (g.cm^{-3})	*1.307*	*1.325*	*1.365*	*1.270*
Crystal system	Monoclinic	Monoclinic	Triclinic	Triclinic
Space group	P 21/c	P 21/c	P -1	P -1
T (K)	100	100	100	100
Wavelength Mo-Kα (Å)	0.71073	0.71073	0.71073	0.71073
μ (mm^{-1})	0.239	0.243	0.223	0.251
F (000)	*1072.0*	*1072.0*	*456.0*	*616.0*
θ max (°)	30.692	25.026	30.595	28.378
h, k, l max	17, 23, 17	13, 26, 11	15, 16, 16	13, 15, 19
Reflections collected	7975	4479	6482	7593
Independant reflections	6147	2895	5123	5934
Data completeness	0.998	0.997	0.998	0.997
Goodness-of-fit on F^2	1.031	1.149	1.051	1.080
R indices (all data)	R = 0.0465	R = 0.1011	R = 0.0418	R = 0.0415
	wR2 = 0.1237	wR2 = 0.1922	wR2 = 0.1026	wR2 = 0.1005

Table S1: Crystallographic table of $^{n}(Si_3O)_2SiPc$ polymorph 1 and 2, $(Si_2O)_2SiPc$ and $(Si_4O)_2SiPc$

Table S2: Average electrical characteristics of $(Si_XO)_2SiPc$ OTFTs prepared using different annealing temperatures, calculated from N unique transistors.

Compound	Annealing temperature (°C)	$\mu_{h,avg}$ ($cm^2V^{-1}s^{-1}$)[a]	V_T[b]	$I_{on/off}$[c]	N[d]
$(Si_2O)_2SiPc$	/	5.8 (± 1.8) x10^{-2}	- 35.4 (± 1.7)	10^3	19
	80	7.2 (± 1.4) x10^{-2}	- 31.9 (± 2.8)	10^4	19
	120	2.3 (± 2.0) x10^{-2}	- 34.4 (± 2.8)	10^3	17
	160	3.7 (± 0.7) x10^{-2}	- 36.3 (± 3.3)	10^3	17
$^n(Si_3O)_2SiPc$	/	1.3 (± 0.5) x10^{-3}	- 41.8 (± 5.6)	10^2	17
	80	3.4 (± 1.4) x10^{-3}	- 45.2 (± 4.1)	10^2	19
	120	1.7 (± 0.5) x10^{-3}	- 43.4 (± 3.0)	10^2	18
	160	1.4 (± 1.6) x10^{-3}	- 38.9 (± 2.2)	10^2	18
$^{iso}(Si_3O)_2SiPc$[e]	/	0.32 (± 0.10)	- 18.7 (± 9.4)	10^5	17
	80	0.73 (± 0.25)	-18.2 (± 3.9)	10^5	13
	120	0.55 (± 0.12)	- 19.4 (± 3.0)	10^5	15
	160	1.01 (± 0.16)	- 15.9 (± 3.0)	10^5	18
$(Si_4O)_2SiPc$	/	0.14 (± 0.05)	- 28.6 (± 4.9)	10^5	15
	80	3.6 (± 1.8) x10^{-2}	- 32.8 (± 2.0)	10^3	18
	120	7.5 (± 3.4) x10^{-2}	- 34.1 (± 1.7)	10^4	18
	160	0.21 (± 0.08)	- 32.2 (± 1.9)	10^5	17

[a]Average saturation regime hole field-effect mobility ($\mu_{h,avg}$). [b]Mean threshold voltage (V_T). [c]On/off current ratio. [d]Number of unique transistors used for calculation of the averages; All devices were made with gold electrodes using BGTC configuration, measurements were conducted in air with V_{DS} = -50 V. Characteristic output and transfer curves for each new condition can be found in the ESI (**Figure S33-44**). [e]All the data for **$^{iso}(Si_3O)_2SiPc$** were taken from Ledos et al.[1]

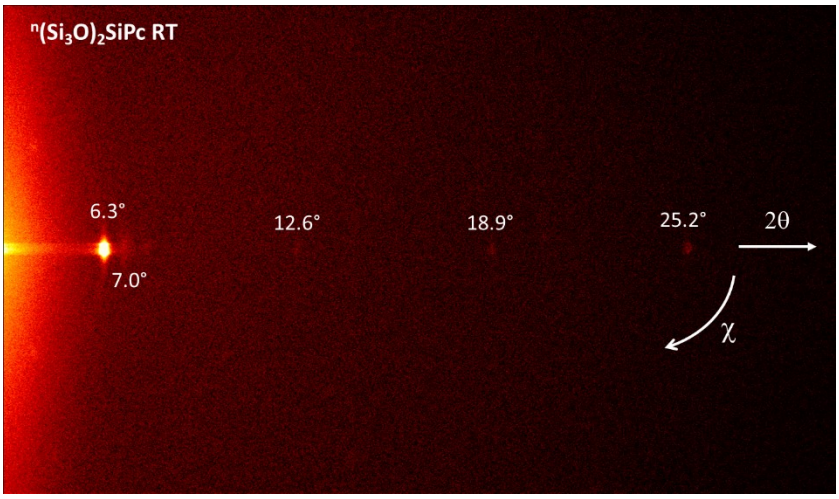

Figure S9: 2D-PXRD map of **$^n(Si_3O)_2SiPc$** thin film on ODTS-treated SiO_2 surfaces. The map ranges from 2θ = 3° to 30° on the Y-axis, from the left to the right.

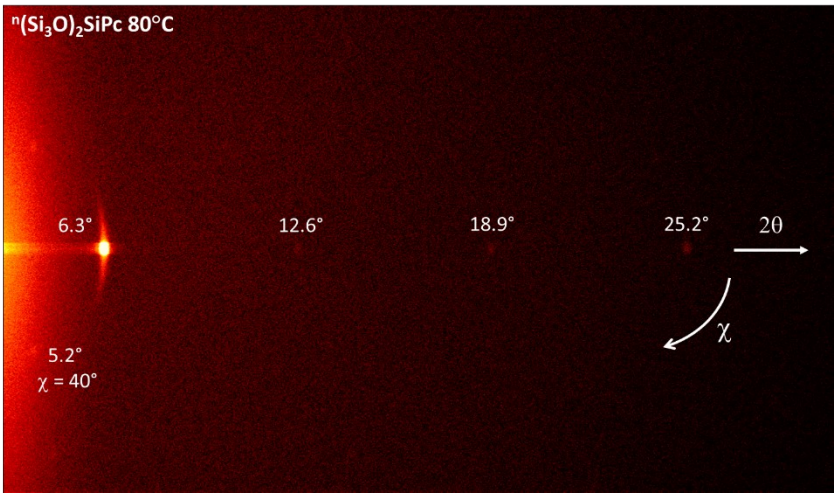

Figure S10: 2D-PXRD map of **$^{n}(Si_3O)_2SiPc$** thin film on ODTS-treated SiO_2 surfaces annealed at 80°C. The map ranges from 2θ = 3° to 30° on the Y-axis, from the left to the right.

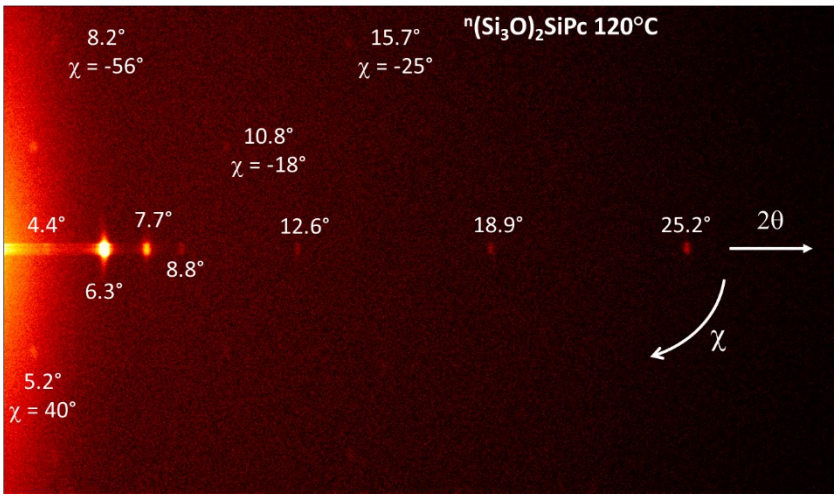

Figure S11: 2D-PXRD map of **$^{n}(Si_3O)_2SiPc$** thin film on ODTS-treated SiO_2 surfaces annealed at 120°C. The map ranges from 2θ = 3° to 30° on the Y-axis, from the left to the right.

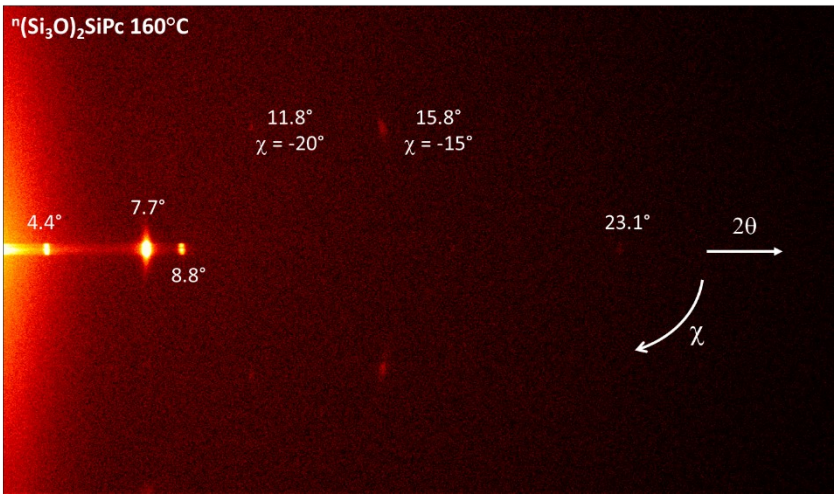

Figure S12: 2D-PXRD map of **$^{n}(Si_3O)_2SiPc$** thin film on ODTS-treated SiO_2 surfaces annealed at 160°C. The map ranges from 2θ = 3° to 30° on the Y-axis, from the left to the right.

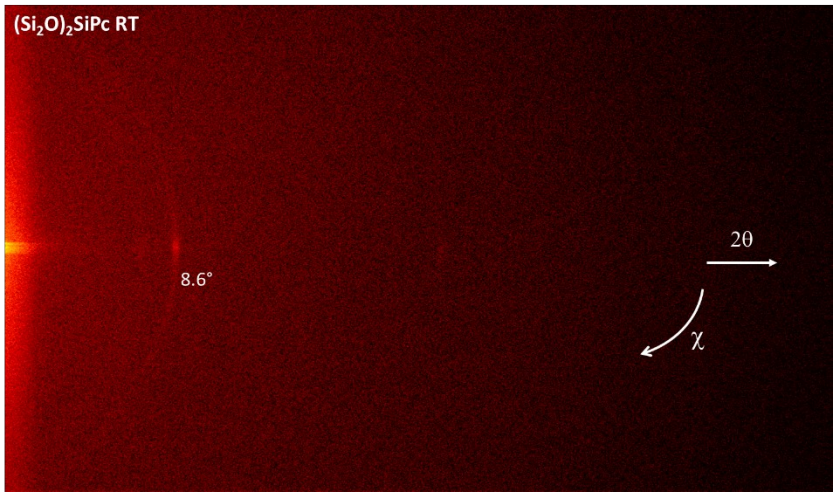

Figure S13: 2D-PXRD map of **$(Si_2O)_2SiPc$** thin film on ODTS-treated SiO_2 surfaces. The map ranges from 2θ = 3° to 30° on the Y-axis, from the left to the right.

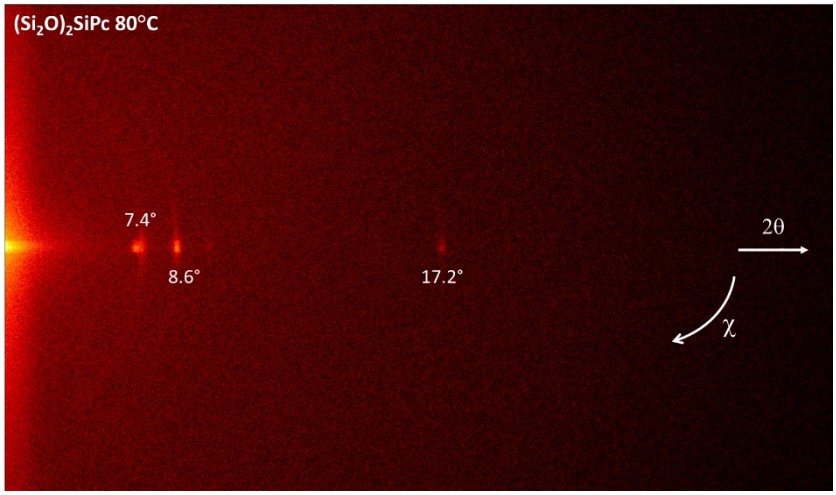

Figure S14: 2D-PXRD map of **$(Si_2O)_2SiPc$** thin film on ODTS-treated SiO_2 surfaces annealed at 80°C. The map ranges from 2θ = 3° to 30° on the Y-axis, from the left to the right.

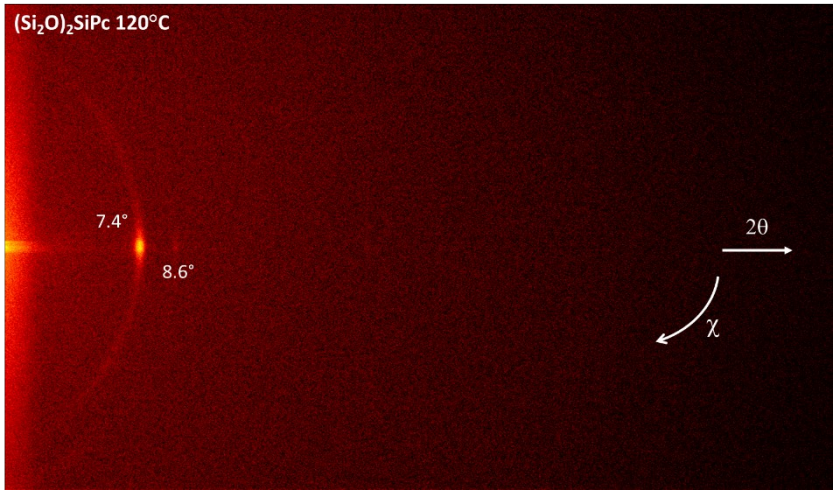

Figure S15: 2D-PXRD map of **$(Si_2O)_2SiPc$** thin film on ODTS-treated SiO_2 surfaces annealed at 120°C. The map ranges from 2θ = 3° to 30° on the Y-axis, from the left to the right.

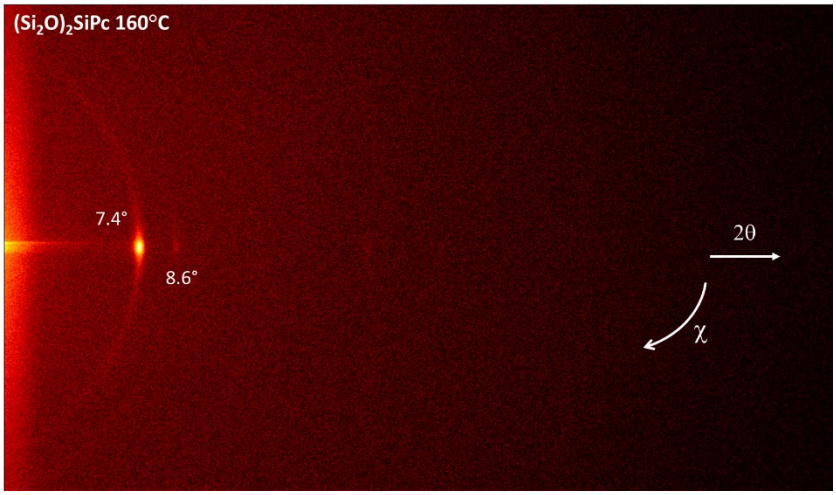

Figure S16: 2D-PXRD map of **$(Si_2O)_2SiPc$** thin film on ODTS-treated SiO_2 surfaces annealed at 160°C. The map ranges from 2θ = 3° to 30° on the Y-axis, from the left to the right.

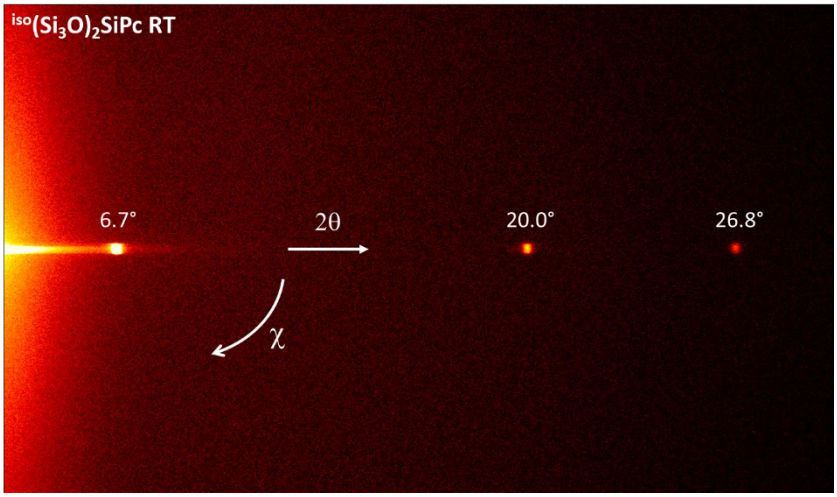

Figure S17: 2D-PXRD map of **$^{iso}(Si_3O)_2SiPc$** thin film on ODTS-treated SiO_2 surfaces. The map ranges from 2θ = 3° to 30° on the Y-axis, from the left to the right.

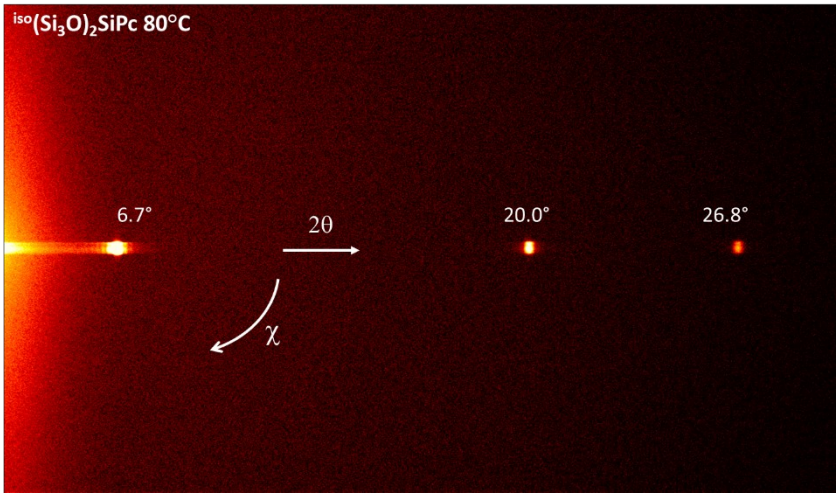

Figure S18: 2D-PXRD map of **$^{iso}(Si_3O)_2SiPc$** thin film on ODTS-treated SiO_2 surfaces annealed at 80°C. The map ranges from 2θ = 3° to 30° on the Y-axis, from the left to the right.

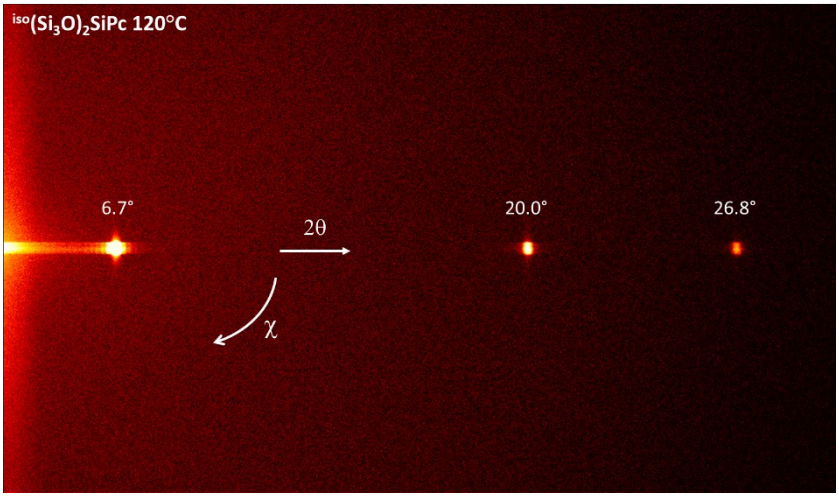

Figure S19: 2D-PXRD map of **$^{iso}(Si_3O)_2SiPc$** thin film on ODTS-treated SiO_2 surfaces annealed at 120°C. The map ranges from 2θ = 3° to 30° on the Y-axis, from the left to the right.

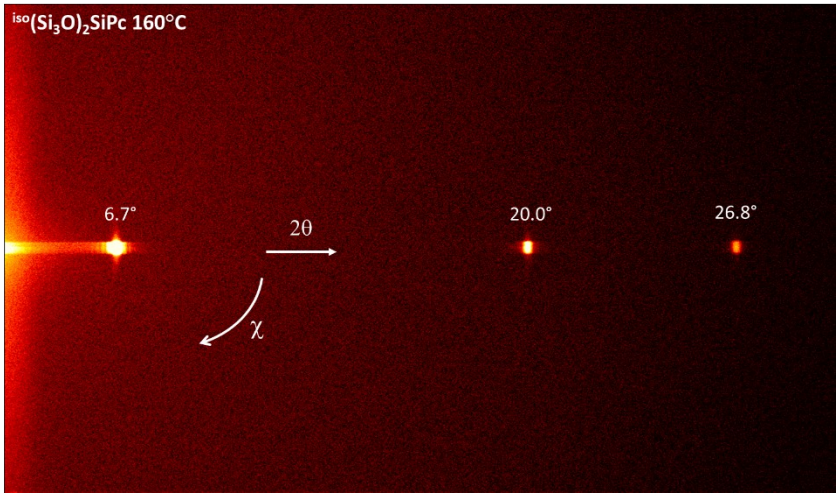

Figure S20: 2D-PXRD map of **$^{iso}(Si_3O)_2SiPc$** thin film on ODTS-treated SiO_2 surfaces annealed at 160°C. The map ranges from 2θ = 3° to 30° on the Y-axis, from the left to the right.

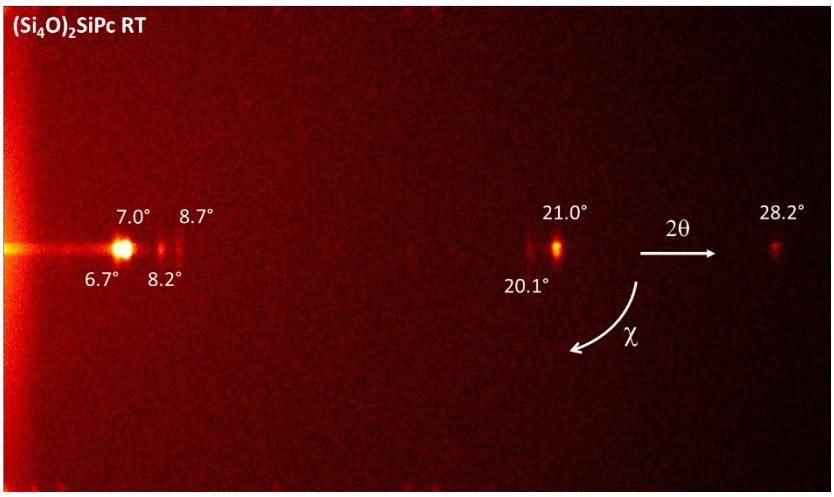

Figure S21: 2D-PXRD map of **$(Si_4O)_2SiPc$** thin film on ODTS-treated SiO_2 surfaces. The map ranges from 2θ = 3° to 30° on the Y-axis, from the left to the right.

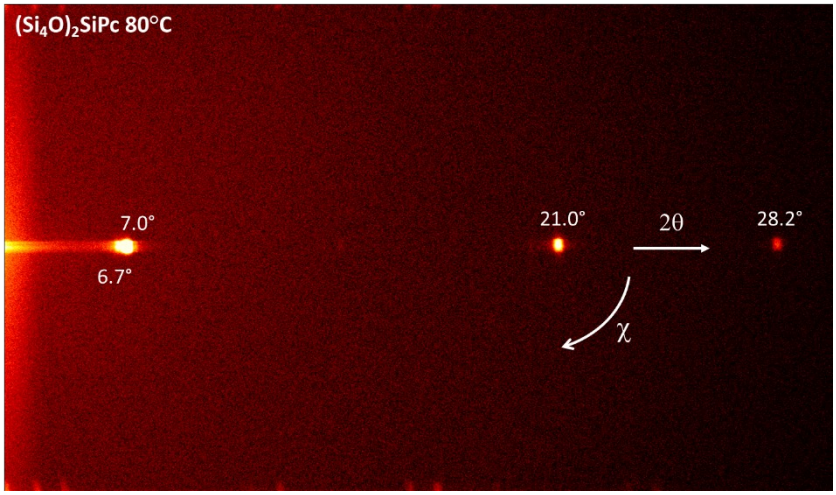

Figure S22: 2D-PXRD map of **$(Si_4O)_2SiPc$** thin film on ODTS-treated SiO_2 surfaces annealed at 80°C. The map ranges from 2θ = 3° to 30° on the Y-axis, from the left to the right.

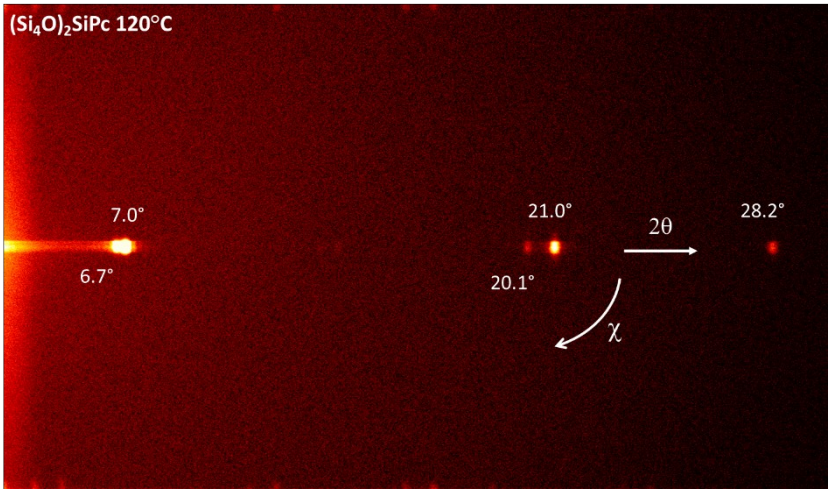

Figure S23: 2D-PXRD map of **$(Si_4O)_2SiPc$** thin film on ODTS-treated SiO_2 surfaces annealed at 120°C. The map ranges from 2θ = 3° to 30° on the Y-axis, from the left to the right.

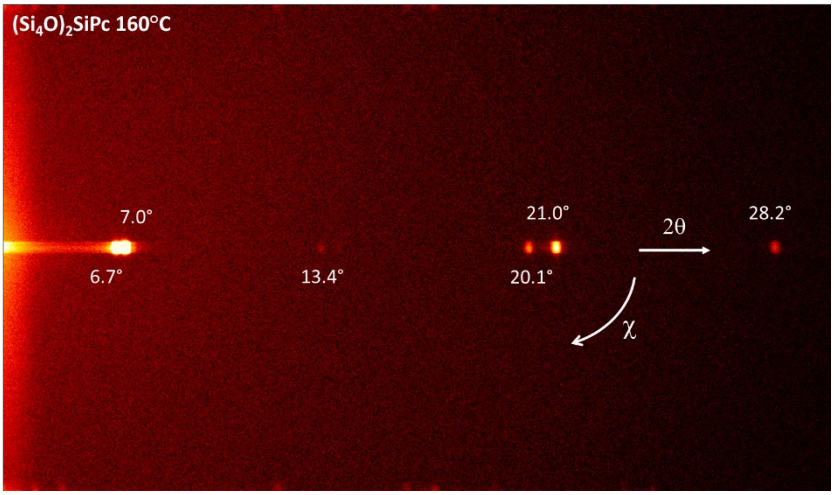

Figure S24: 2D-PXRD map of **$(Si_4O)_2SiPc$** thin film on ODTS-treated SiO_2 surfaces annealed at 160°C. The map ranges from 2θ = 3° to 30° on the Y-axis, from the left to the right.

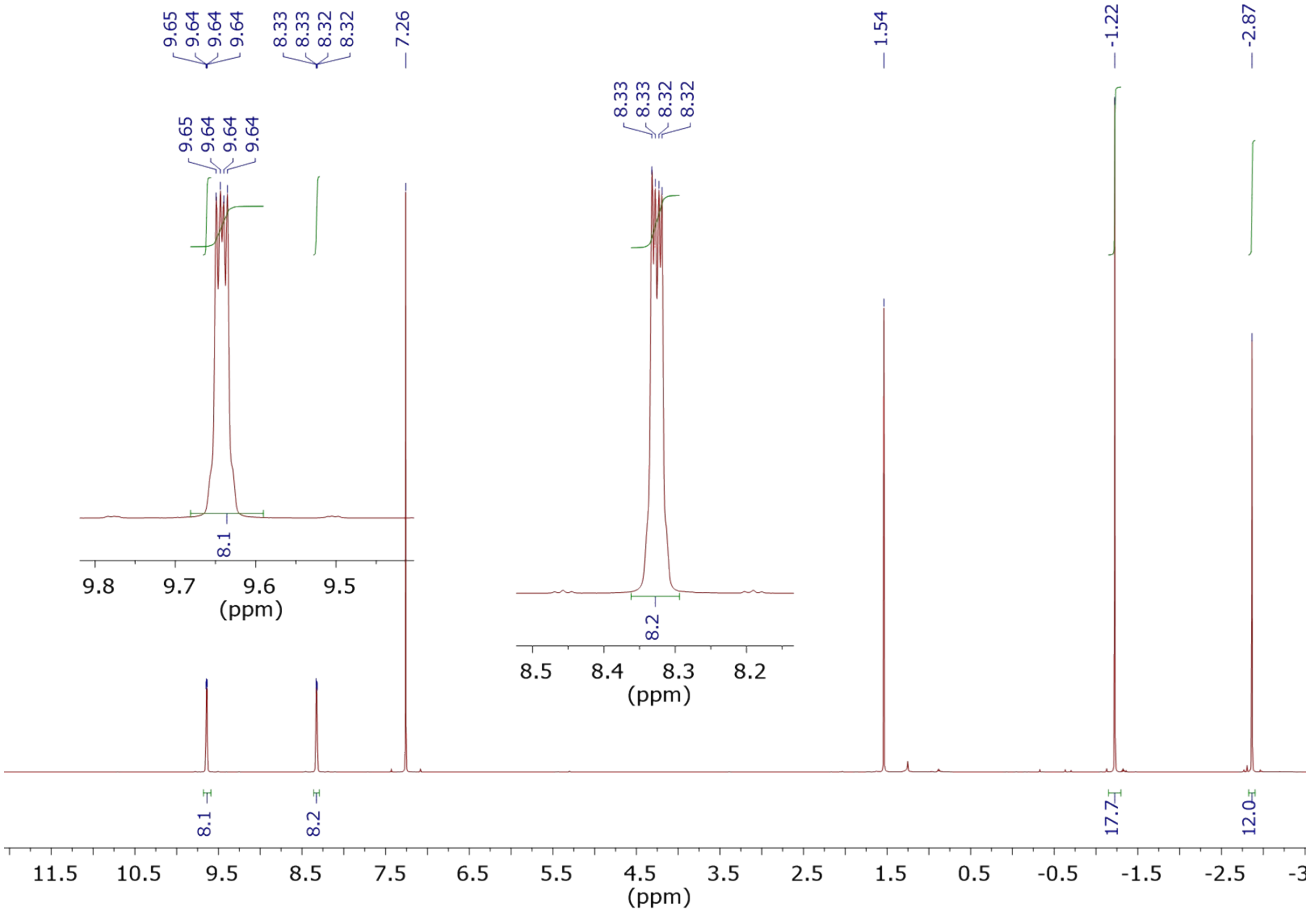

Figure S25: ^{1}H NMR of a **$(Si_2O)_2SiPc$** solution in $CDCl_3$.

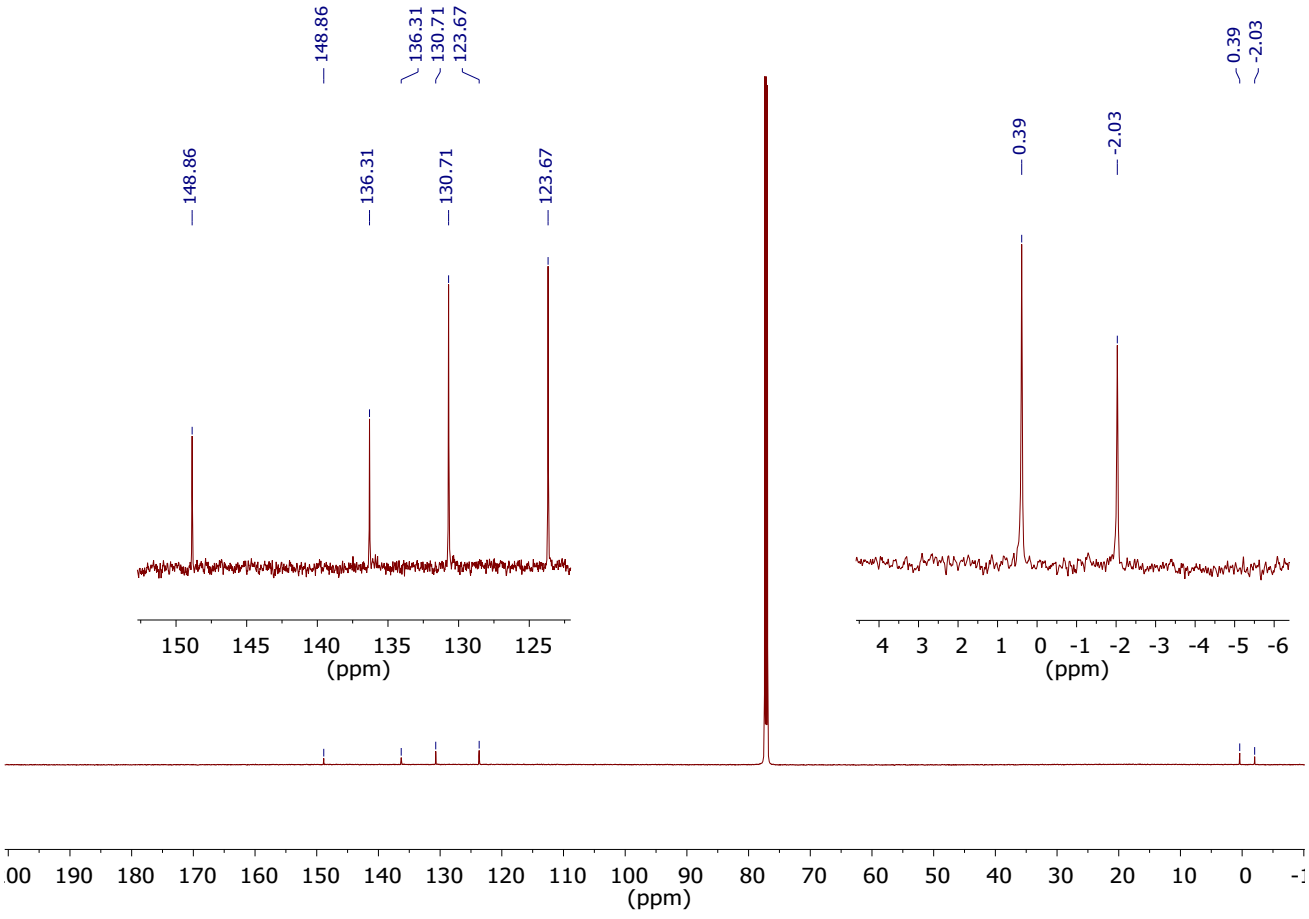

Figure S26: ^{13}C NMR of a **$(Si_2O)_2SiPc$** solution in $CDCl_3$.

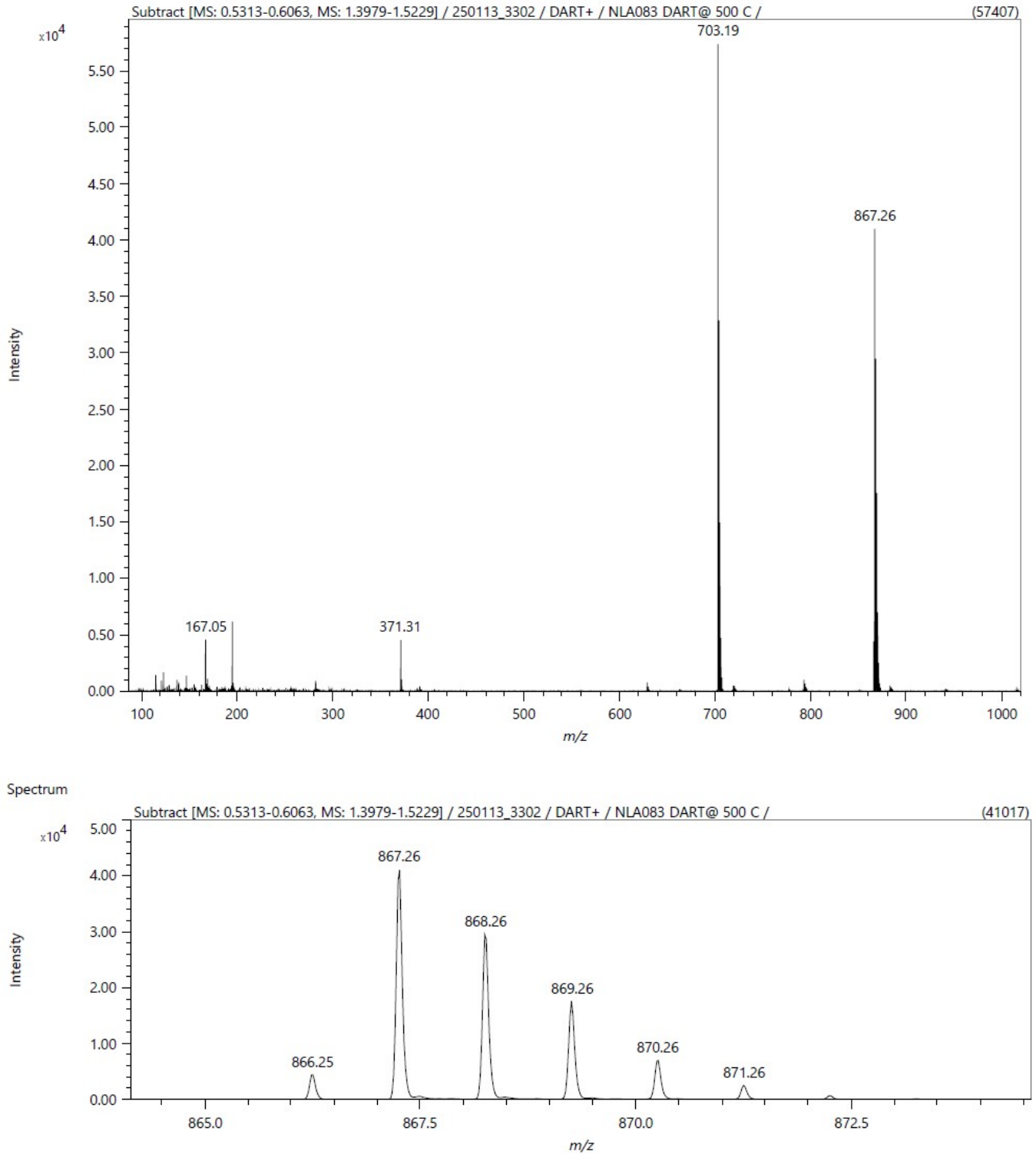

Figure S27: HRMS of **$(Si_2O)_2SiPc$**

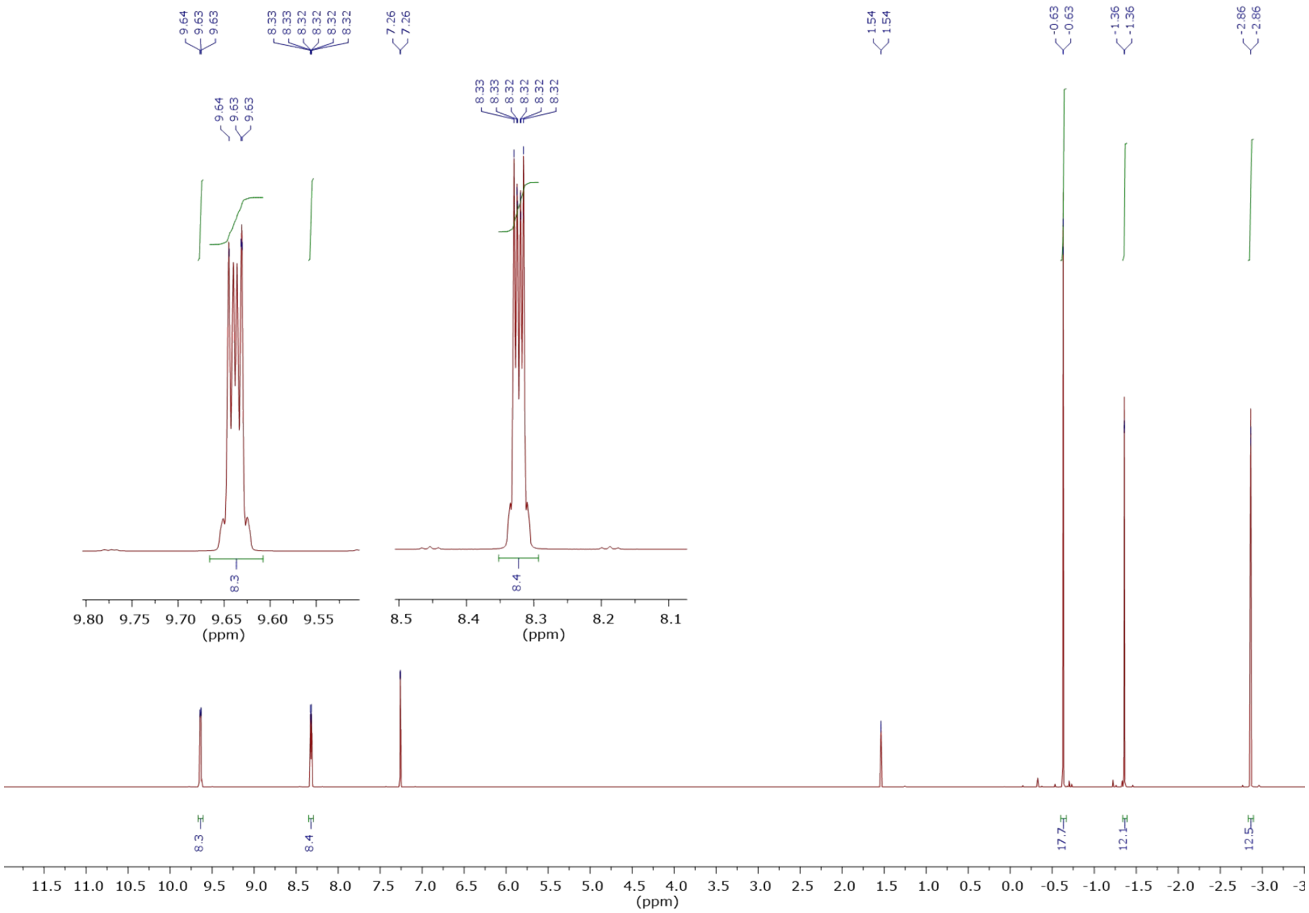

Figure S28: ^{1}H NMR of a **^{n}(Si$_3$O)$_2$SiPc** solution in $CDCl_3$.

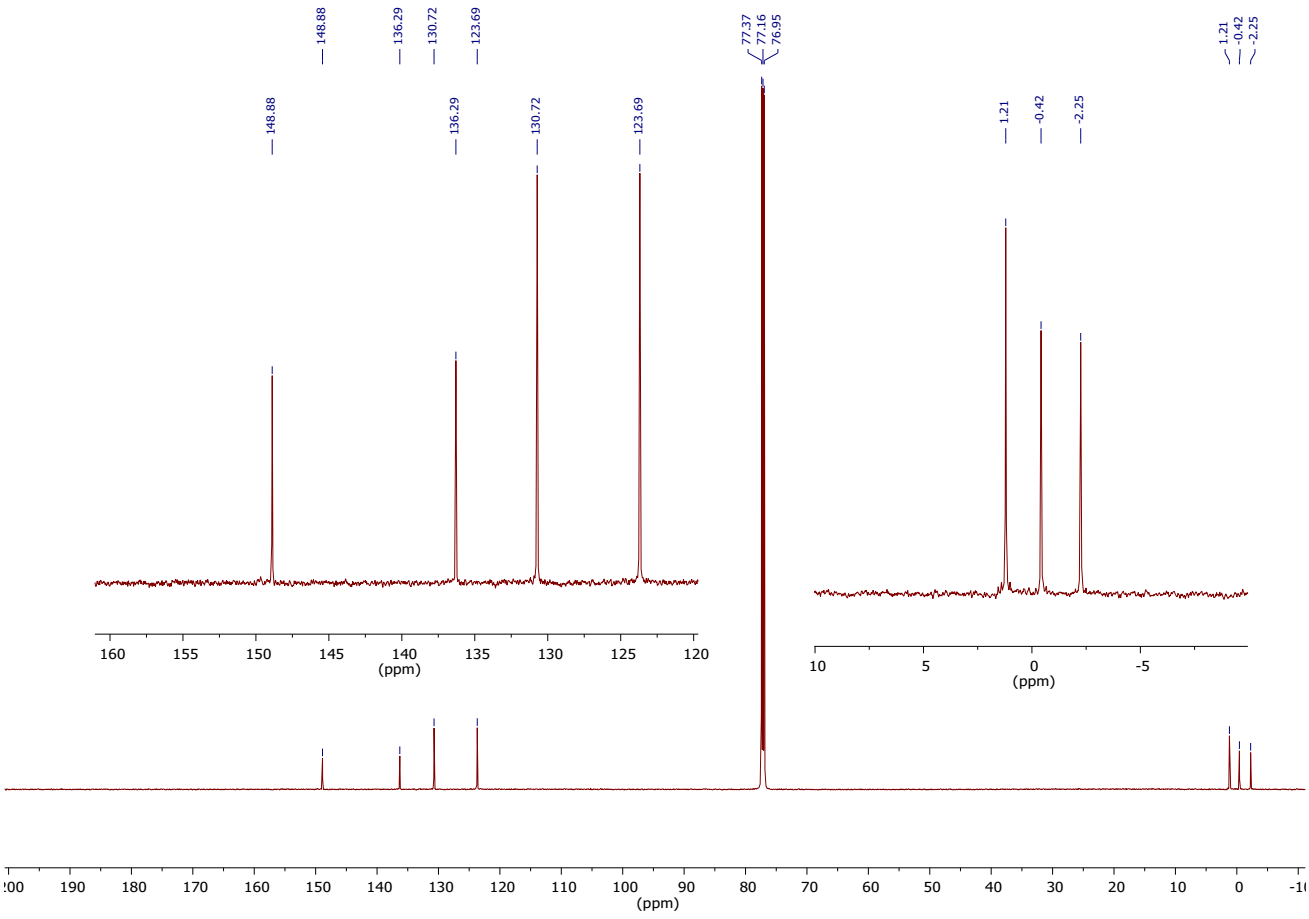

Figure S29: ^{13}C NMR of a **^{n}(Si$_3$O)$_2$SiPc** solution in $CDCl_3$.

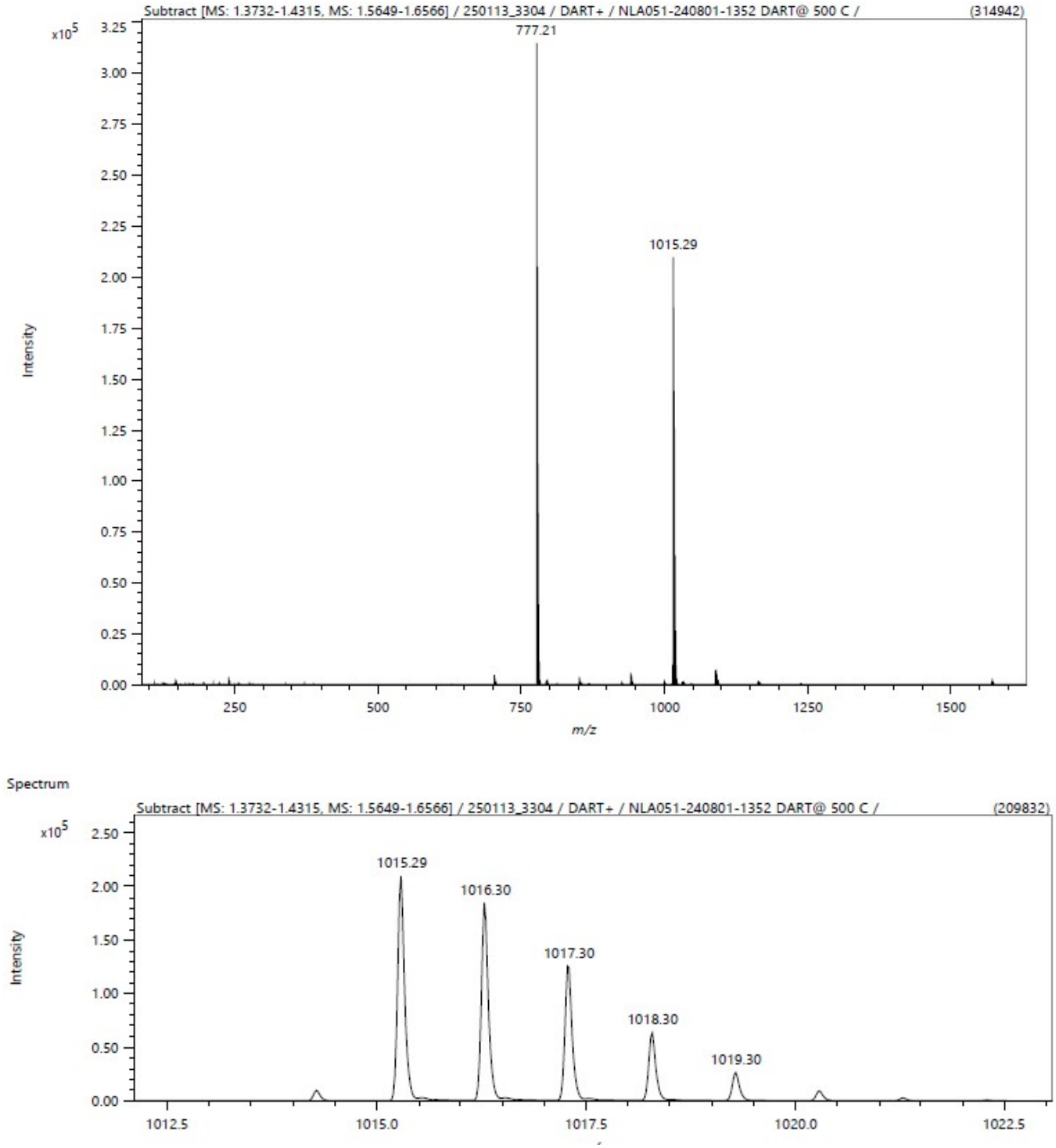

Figure S30: HRMS of **$^{n}(Si_3O)_2SiPc$**

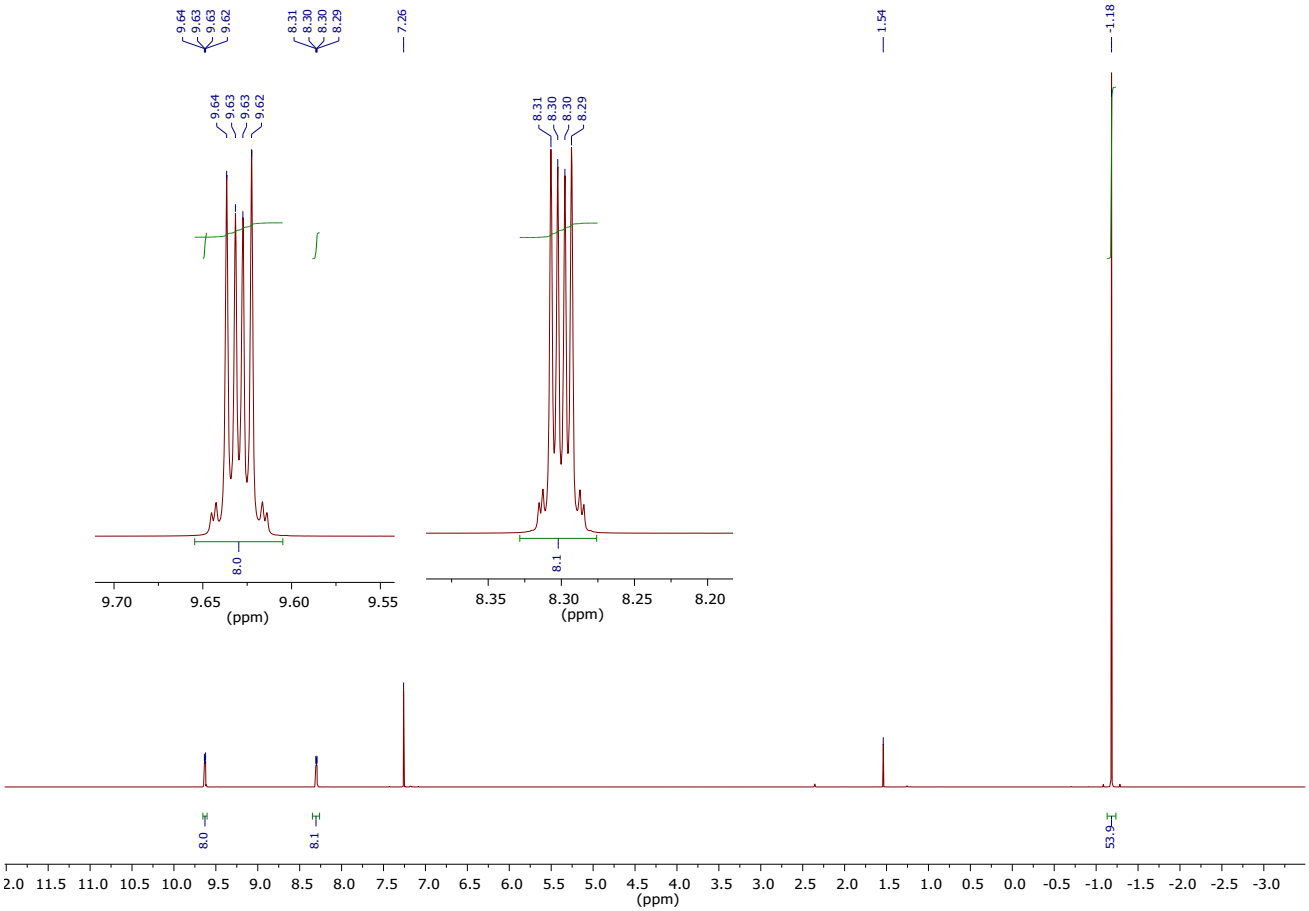

Figure S31: ^{1}H NMR of a **$(Si_4O)_2SiPc$** solution in $CDCl_3$.

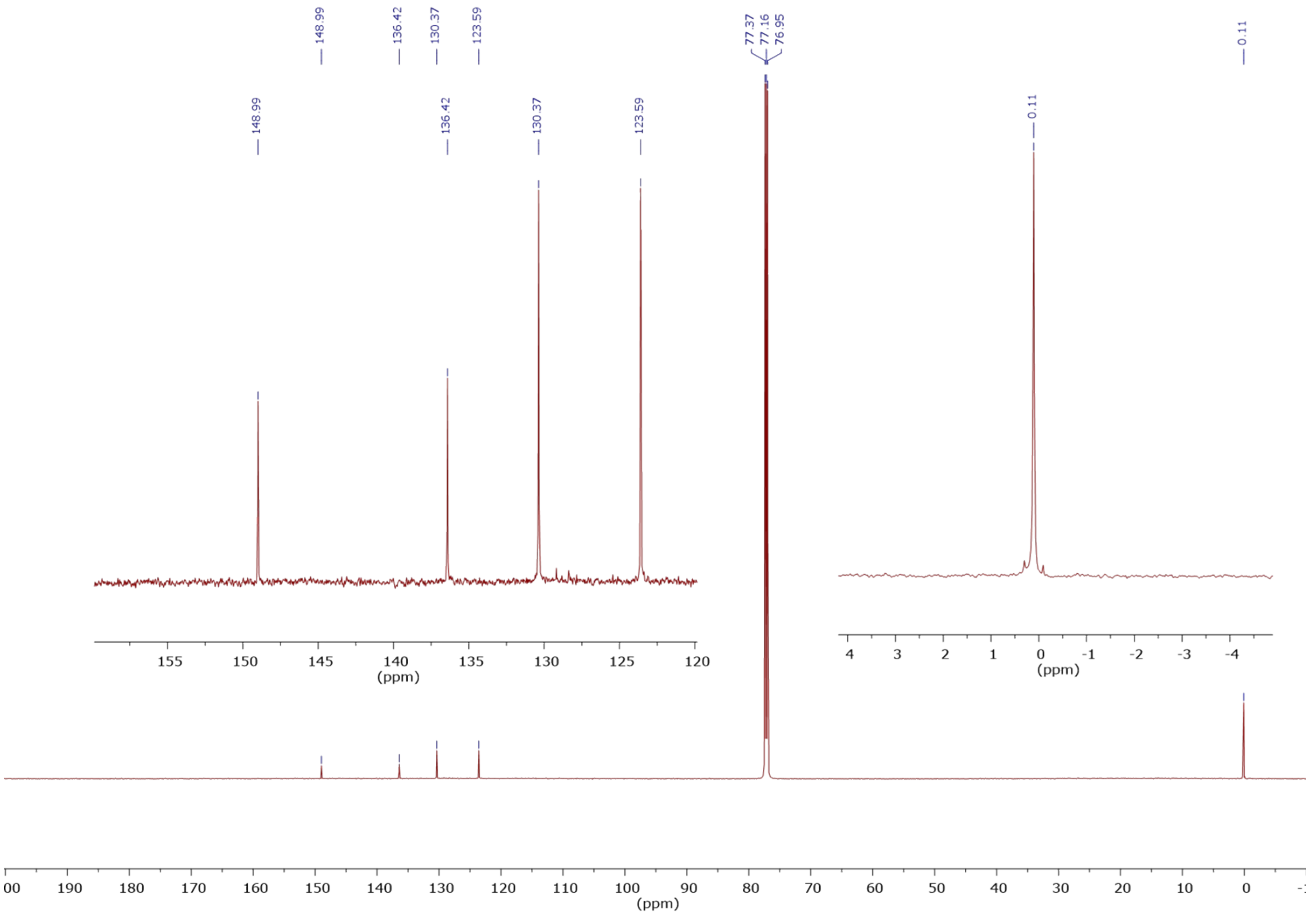

Figure S32: ^{13}C NMR of a **$(Si_4O)_2SiPc$** solution in $CDCl_3$.

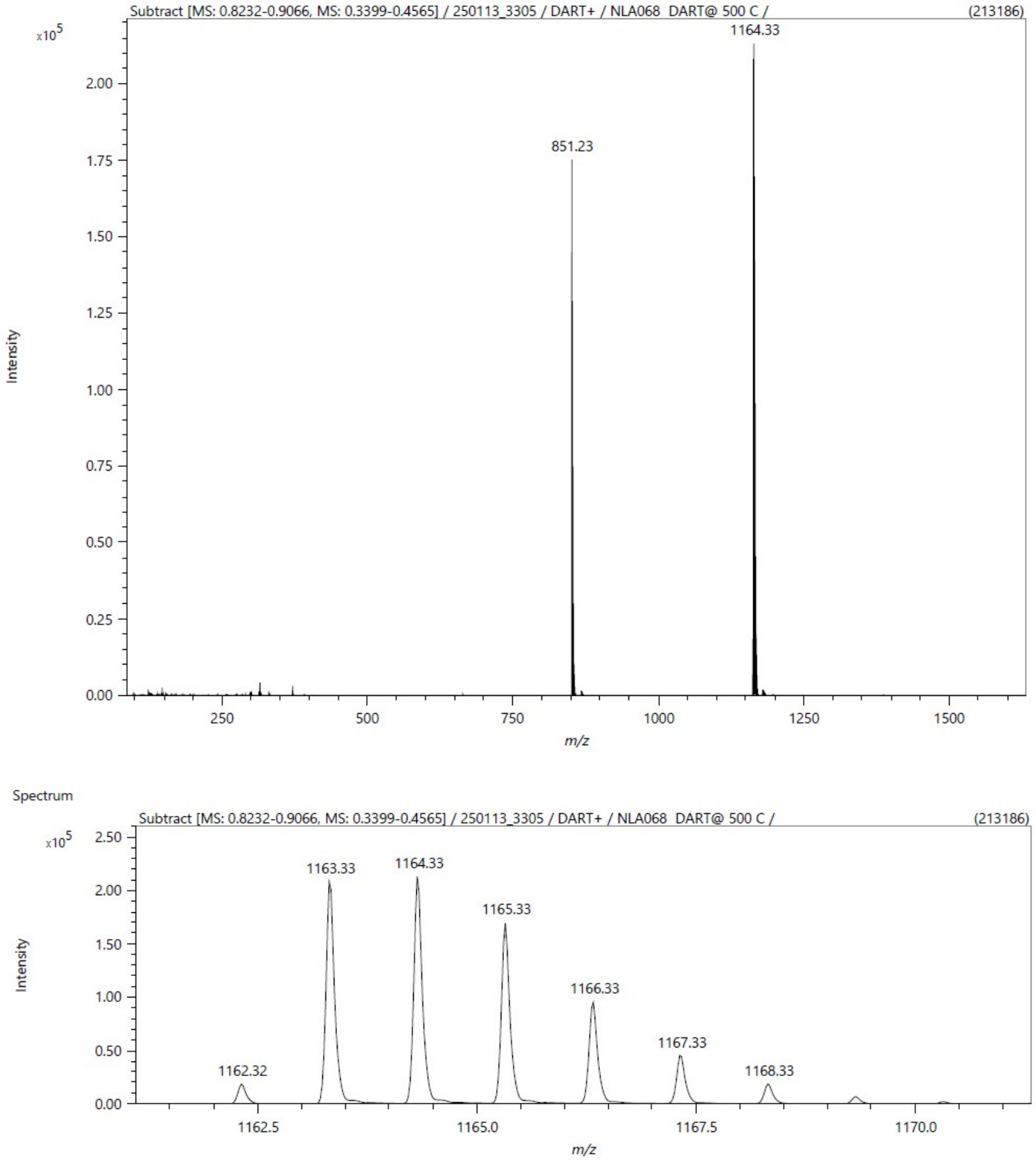

Figure S33: HRMS of **$(Si_4O)_2SiPc$**

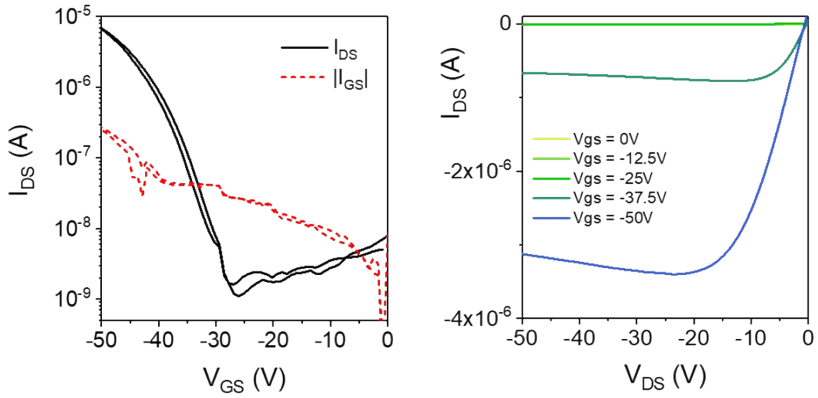

Figure S34: Output curves for **$(Si_2O)_2SiPc$** deposited on plasma ODTS-treated SiO_2 surface in BGTC OTFTs with a channel length of 30 µm and a channel width of 1000 µm measured in air alongside the corresponding transfer curves (V_{DS}= -50 V). S-D electrodes were made out of gold.

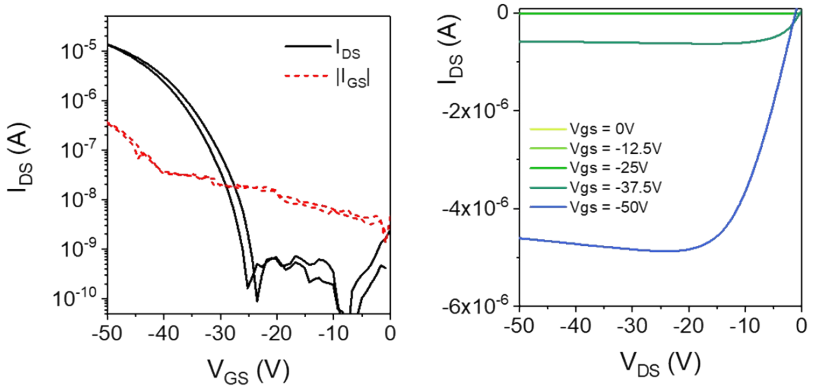

Figure S35: Output curves for **$(Si_2O)_2SiPc$** deposited on plasma ODTS-treated SiO_2, **annealed at 80°C**, surface in BGTC OTFTs with a channel length of 30 µm and a channel width of 1000 µm measured in air alongside the corresponding transfer curves (V_{DS}= -50 V). S-D electrodes were made out of gold.

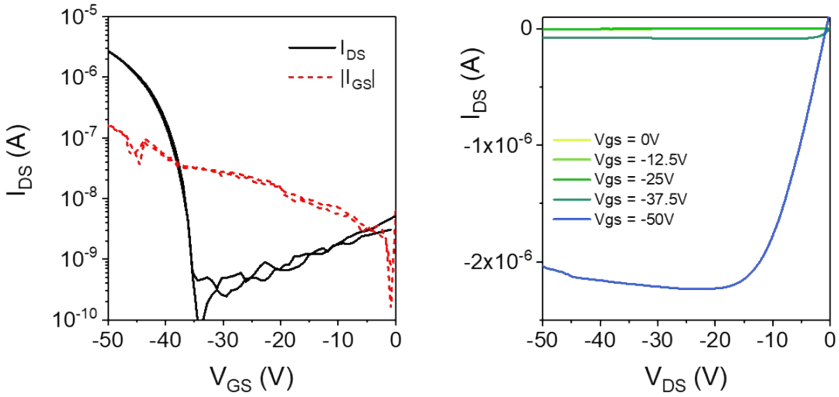

Figure S36: Output curves for **$(Si_2O)_2SiPc$** deposited on plasma ODTS-treated SiO_2, **annealed at 120°C**, surface in BGTC OTFTs with a channel length of 30 µm and a channel width of 1000 µm measured in air alongside the corresponding transfer curves (V_{DS}= -50 V). S-D electrodes were made out of gold.

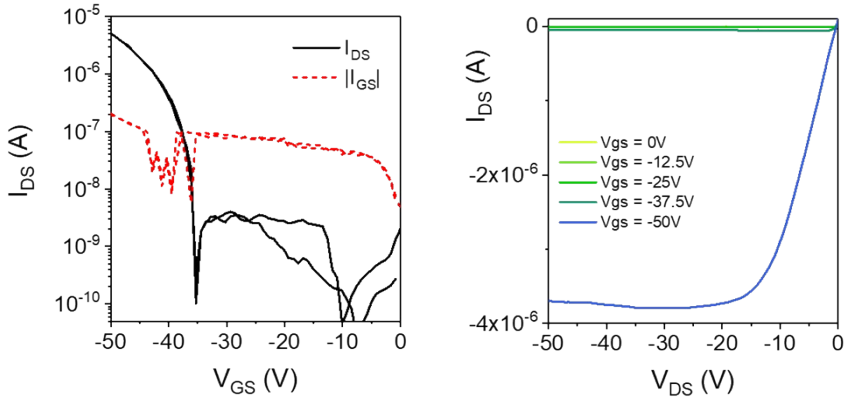

Figure S37: Output curves for **$(Si_2O)_2SiPc$** deposited on plasma ODTS-treated SiO_2, **annealed at 160°C**, surface in BGTC OTFTs with a channel length of 30 µm and a channel width of 1000 µm measured in air alongside the corresponding transfer curves (V_{DS}= -50 V). S-D electrodes were made out of gold.

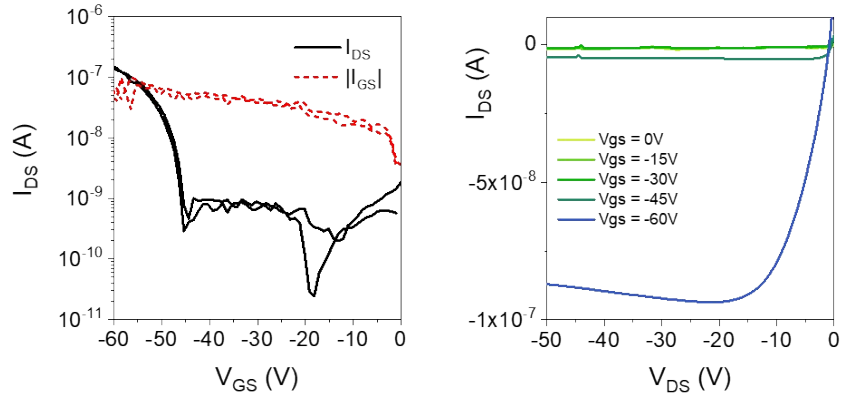

Figure S38: Output curves for **$^n(Si_3O)_2SiPc$** deposited on plasma ODTS-treated SiO_2 surface in BGTC OTFTs with a channel length of 30 µm and a channel width of 1000 µm measured in air alongside the corresponding transfer curves (V_{DS}= -50 V). S-D electrodes were made out of gold.

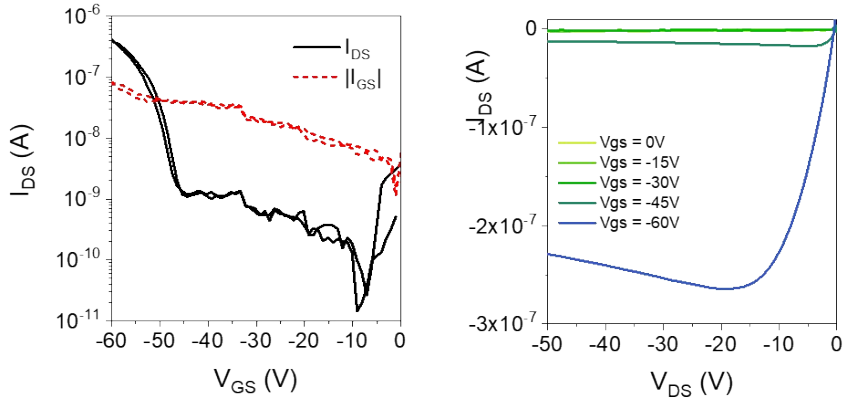

Figure S39: Output curves for **$^n(Si_3O)_2SiPc$** deposited on plasma ODTS-treated SiO_2, **annealed at 80°C**, surface in BGTC OTFTs with a channel length of 30 µm and a channel width of 1000 µm measured in air alongside the corresponding transfer curves (V_{DS}= -50 V). S-D electrodes were made out of gold.

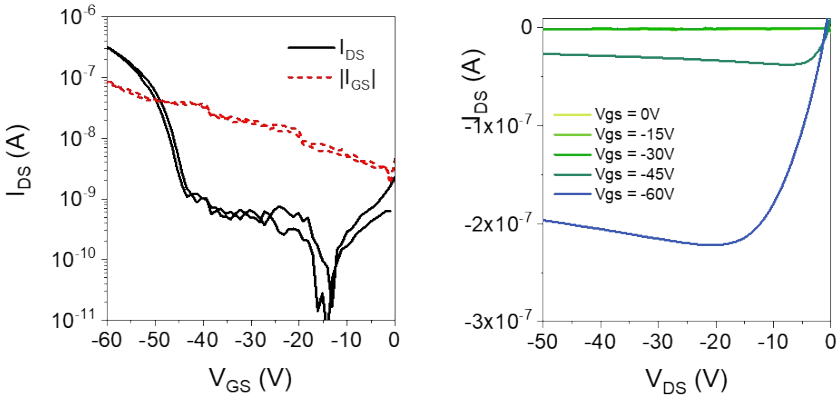

Figure S40: Output curves for **$^{n}(Si_3O)_2SiPc$** deposited on plasma ODTS-treated SiO_2, **annealed at 120°C**, surface in BGTC OTFTs with a channel length of 30 µm and a channel width of 1000 µm measured in air alongside the corresponding transfer curves (V_{DS}= -50 V). S-D electrodes were made out of gold.

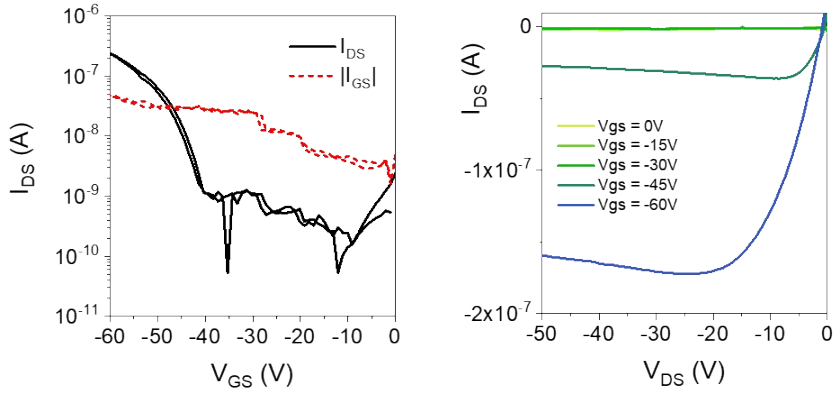

Figure S41: Output curves for **$^{n}(Si_3O)_2SiPc$** deposited on plasma ODTS-treated SiO_2, **annealed at 160°C**, surface in BGTC OTFTs with a channel length of 30 µm and a channel width of 1000 µm measured in air alongside the corresponding transfer curves (V_{DS}= -50 V). S-D electrodes were made out of gold.

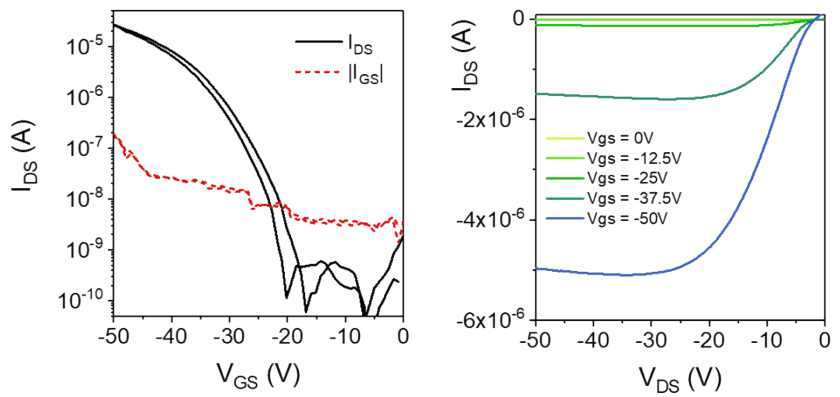

Figure S42: Output curves for **$(Si_4O)_2SiPc$** deposited on plasma ODTS-treated SiO_2 surface in BGTC OTFTs with a channel length of 30 µm and a channel width of 1000 µm measured in air alongside the corresponding transfer curves (V_{DS}= -50 V). S-D electrodes were made out of gold.

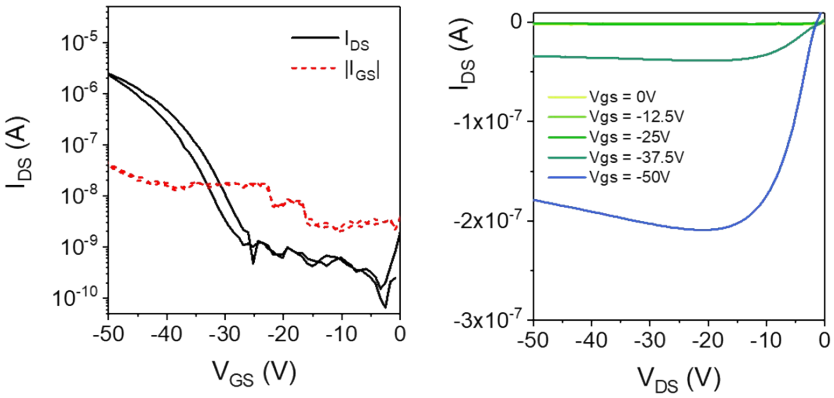

Figure S43: Output curves for **$(Si_4O)_2$SiPc** deposited on plasma ODTS-treated SiO_2, **annealed at 80°C**, surface in BGTC OTFTs with a channel length of 30 µm and a channel width of 1000 µm measured in air alongside the corresponding transfer curves (V_{DS}= -50 V). S-D electrodes were made out of gold.

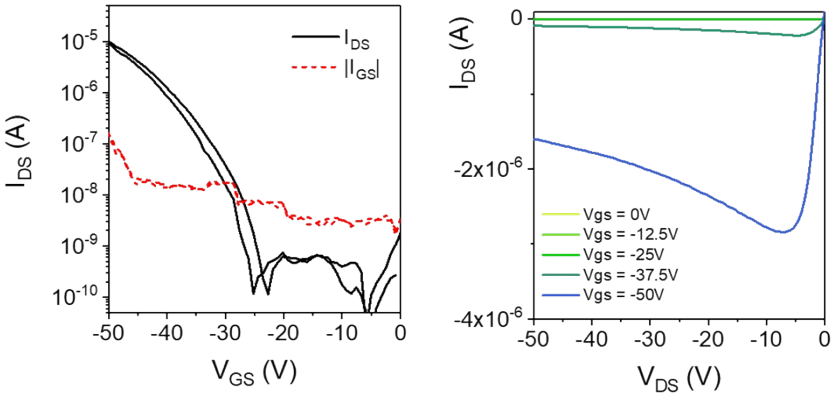

Figure S44: Output curves for **$(Si_4O)_2$SiPc** deposited on plasma ODTS-treated SiO_2, **annealed at 120°C**, surface in BGTC OTFTs with a channel length of 30 µm and a channel width of 1000 µm measured in air alongside the corresponding transfer curves (V_{DS}= -50 V). S-D electrodes were made out of gold.

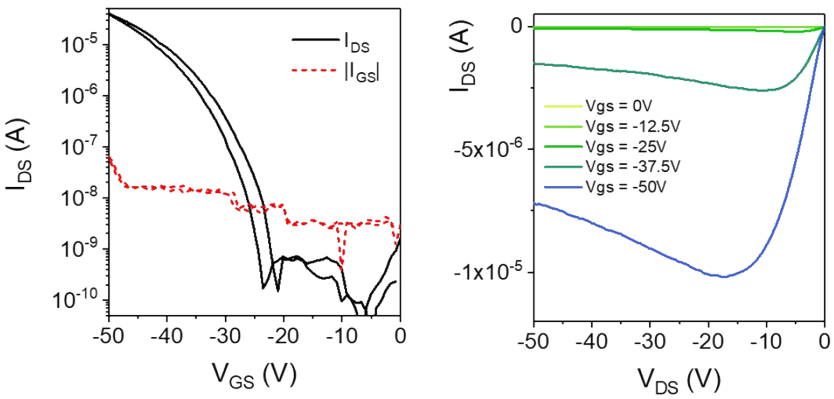

Figure S45: Output curves for **$(Si_4O)_2$SiPc** deposited on plasma ODTS-treated SiO_2, **annealed at 160°C**, surface in BGTC OTFTs with a channel length of 30 µm and a channel width of 1000 µm measured in air alongside the corresponding transfer curves (V_{DS}= -50 V). S-D electrodes were made out of gold.

References

(1) Ledos, N.; Lamontagne, H. R.; Manion, J.; Castet, F.; Lessard, B. H.; Brusso, J. L. Siloxane-Functionalized Silicon Phthalocyanine OTFTs: High Hole Mobility and Unexpected p-Type Character. *Advanced Functional Materials n/a* (n/a), e14609. https://doi.org/10.1002/adfm.202514609.

(2) Vebber, M. C.; Grant, T. M.; Brusso, J. L.; Lessard, B. H. Bis(Trialkylsilyl Oxide) Silicon Phthalocyanines: Understanding the Role of Solubility in Device Performance as Ternary Additives in Organic Photovoltaics. *Langmuir* **2020**, *36* (10), 2612–2621. https://doi.org/10.1021/acs.langmuir.9b03772.

(3) Cranston, R. R.; Vebber, M. C.; Berbigier, J. F.; Rice, N. A.; Tonnelé, C.; Comeau, Z. J.; Boileau, N. T.; Brusso, J. L.; Shuhendler, A. J.; Castet, F.; Muccioli, L.; Kelly, T. L.; Lessard, B. H. Thin-Film Engineering of Solution-Processable n-Type Silicon Phthalocyanines for Organic Thin-Film Transistors. *ACS Appl. Mater. Interfaces* **2021**, *13* (1), 1008–1020. https://doi.org/10.1021/acsami.0c17657.

(4) Vebber, M. C.; Rice, N. A.; Brusso, J. L.; Lessard, B. H. Thermodynamic Property–Performance Relationships in Silicon Phthalocyanine-Based Organic Photovoltaics. *ACS Appl. Energy Mater.* **2022**, *5* (3), 3426–3435. https://doi.org/10.1021/acsaem.1c04013.

(5) Cranston, R. R.; Vebber, M. C.; Rice, N. A.; Tonnelé, C.; Castet, F.; Muccioli, L.; Brusso, J. L.; Lessard, B. H. N-Type Solution-Processed Tin versus Silicon Phthalocyanines: A Comparison of Performance in Organic Thin-Film Transistors and in Organic Photovoltaics. *ACS Appl. Electron. Mater.* **2021**, *3* (4), 1873–1885. https://doi.org/10.1021/acsaelm.1c00114.

(6) Noll, W. *Chemistry and Technology of Silicones*; Academic Press, 2012.